

# SEISMIC PROPAGATION FROM ACTIVITY IN TUNNELS AND UNDERGROUND FACILITIES

Stephen A. Ketcham\*, Jason R. McKenna, Roy J. Greenfield, and Thomas S. Anderson  
US Army Engineer Research and Development Center, Hanover, NH, 03755

## ABSTRACT

Dynamic mechanical activity in a tunnel can be measured as ground vibrations at offset distances. These signals can be processed in sensing algorithms for detection, location, and discrimination of the activity. The objective of this work is to demonstrate that seismic simulations can reveal the effect of the environment on seismic energy as it propagates from tunnels. Using massively parallel high-performance computers, the work applies a finite-difference solution to the equations of motion and isotropic stress-velocity for viscoelastic seismic propagation. Results from simulations in open, urban, and mountainous terrain reveal the nature of seismic waves as they propagate from tunnel-digging pulses and harmonic sources. Measures of relative energy and signal cross correlation provide maps that reveal locations of optimal sensing. We demonstrate applications of beam forming to monitor tunnel activity, and conclude that the simulation method produces realistic wave-field data for clarifying complicated propagation phenomena and for virtual trials of sensing algorithms.

## 1. INTRODUCTION

*“The 105th Military Police Battalion knew something was amiss. What they discovered was breathtaking: a fully completed tunnel that stretched 357 feet, longer than a football field” (Fainaru and Shadid, 2005).*

Detection of clandestine tunnels and underground facilities is a continuing interest of the US DoD (DARPA, 2006), Army (Sabatier and Muir, 2006), and Customs and Border Protection (Rowe, 2006). Research continues in an attempt to find functional and reliable sensing methods, including seismic methods.

Dynamic activity in tunnels emits mechanical energy that propagates away in seismic waves. Resulting ground vibrations can be measured at offset distances and these signals can be used in sensing algorithms for detection, location, and discrimination of the activity. This sensing, referred to as passive seismic detection, is complicated by the topographical, geological, infrastructure, and noise environment of the surrounding area. Our objective in this paper is to demonstrate that high-performance-computing

(HPC) simulations can reveal the effect of the environment on seismic signatures from tunnels, and can produce realistic wave-field data for virtual trials of sensing algorithms and sensor-placement decision tools.

We focus on results from finite-difference time-domain simulations of seismic wave propagation from realistic signature-producing dynamic activity in tunnels, which we model in open, urban, and mountainous terrain. Using broadband sources, we characterize the frequency response of our models, and develop spatial measures of relative energy and cross correlation to perform a virtual trial of optimal sensor placement.

## 2. SEISMIC ANALYSIS METHODOLOGY

The seismic simulation method is a finite-difference time-domain (FDTD) implementation of the equations of motion and isotropic stress-velocity equations for linear-viscoelastic seismic propagation. The formulation applies stretching coordinate transformations, strain-rate velocity relationships, first-order equations of motion, and linear stress-strain via stress-rate-strain-rate equations, to derive variable-grid finite-difference equations (Ketcham, et al., 2005). FORTRAN code performs the computations on HPC machines using four key parallelization features to operate with efficient performance: equal-domain decomposition, MPI, efficient data exchanges at domain overlaps, and MPIIO.

We use second-order spatial finite differences, which allow us to model highly discontinuous material interfaces. We can thus model stress-release at the ground surface and in structural members by directly modeling air in contact with these structures. This method provides flexibility for complex topography and basic urban settings within the limitations of a rectangular grid. The variable grid in turn provides a method to efficiently reduce a rectangular grid’s staircase-interface errors. An absorbing boundary algorithm (Cerjan et al., 1985), used in tandem with a stretched grid adjacent to the model edges, minimizes unwanted reflections from the edges. Seismic sources are introduced through body forces and time series detailing the force history.

Report Documentation Page				Form Approved OMB No. 0704-0188	
Public reporting burden for the collection of information is estimated to average 1 hour per response, including the time for reviewing instructions, searching existing data sources, gathering and maintaining the data needed, and completing and reviewing the collection of information. Send comments regarding this burden estimate or any other aspect of this collection of information, including suggestions for reducing this burden, to Washington Headquarters Services, Directorate for Information Operations and Reports, 1215 Jefferson Davis Highway, Suite 1204, Arlington VA 22202-4302. Respondents should be aware that notwithstanding any other provision of law, no person shall be subject to a penalty for failing to comply with a collection of information if it does not display a currently valid OMB control number.					
1. REPORT DATE <b>01 NOV 2006</b>		2. REPORT TYPE <b>N/A</b>		3. DATES COVERED <b>-</b>	
4. TITLE AND SUBTITLE <b>Seismic Propagation From Activity In Tunnels And Underground Facilities</b>				5a. CONTRACT NUMBER	
				5b. GRANT NUMBER	
				5c. PROGRAM ELEMENT NUMBER	
6. AUTHOR(S)				5d. PROJECT NUMBER	
				5e. TASK NUMBER	
				5f. WORK UNIT NUMBER	
7. PERFORMING ORGANIZATION NAME(S) AND ADDRESS(ES) <b>US Army Engineer Research and Development Center, Hanover, NH, 03755</b>				8. PERFORMING ORGANIZATION REPORT NUMBER	
9. SPONSORING/MONITORING AGENCY NAME(S) AND ADDRESS(ES)				10. SPONSOR/MONITOR'S ACRONYM(S)	
				11. SPONSOR/MONITOR'S REPORT NUMBER(S)	
12. DISTRIBUTION/AVAILABILITY STATEMENT <b>Approved for public release, distribution unlimited</b>					
13. SUPPLEMENTARY NOTES <b>See also ADM002075., The original document contains color images.</b>					
14. ABSTRACT					
15. SUBJECT TERMS					
16. SECURITY CLASSIFICATION OF:			17. LIMITATION OF ABSTRACT <b>UU</b>	18. NUMBER OF PAGES <b>8</b>	19a. NAME OF RESPONSIBLE PERSON
a. REPORT <b>unclassified</b>	b. ABSTRACT <b>unclassified</b>	c. THIS PAGE <b>unclassified</b>			

### 3. RESULTS

In this section we present results of seismic wave propagation from repetitive digging or harmonic mechanical sources inside tunnels within three models. These models are of flat-layered open terrain, urban terrain, and mountainous terrain, respectively. For the latter two models we calculated the frequency response function of the ground surface to broadband sources in the tunnels, and used the response to examine locations for sensor placement. We performed all of the simulations on Cray X1 computers, using multi-streaming processors for efficient stress and particle-velocity computations within the finite-difference time-stepping loop.

#### 3.1. Propagation from tunnel-digging pulses in flat-layered terrain

The first model comprises a flat topographical surface, horizontal layers of soil, a short horizontal tunnel section, and a vertical tunnel shaft open at the surface. Both tunnel sections contain air in contact with the surrounding ground. The soil layers, from the surface downward, include 1.6 m of increasingly stiff sandy soil, 4.6 m of clay, and harder sandy soil. We assigned the viscoelastic material properties and tunnel geometry to approximate near surface soil layers and a constructed tunnel at an experimental site, where the second author has performed digging tests with seismic measurements. Fig. 1a illustrates the model tunnel geometry.

The source in the simulation approximated force pulses caused by a digger with a hand instrument kneeling at the working face of the tunnel (McKenna, 2006; McKenna and McKenna, 2006). Vertical and horizontal force vectors combined to produce a force into the face with a direction 45 degrees downward from horizontal. The source time series was a triangular pulse train with 0.05-s-duration pulses repeating at  $\sim 1$  Hz, with randomness that varied slightly the pulse starting times and resultant-force amplitudes. We discretized the model to produce accurate surface wave propagation for sources having frequency content less than 80 Hz, and filtered the input excitations so they would not exceed this limit.

Fig. 1b contains a snapshot at  $t=0.5$  s of the simulated vertical-particle-velocity field on a vertical cross section through the tunnel. The snapshot time is just after the first pulse application, and the image reveals strong surface waves moving away from the source location and their interference with the shaft. Signals extracted from the simulation data reveal impulsive vertical ground-surface vibrations caused by the surface waves.

Fig. 2b plots simulated vibrations from five digging pulses superimposed on an ambient noise background. The signal is from the surface at 8.6 m from the center of the shaft in the positive easting direction. This location corresponds to the location of the noisy field measurement shown in Fig. 2a, where the digging-pulse frequency was also close to 1 Hz. The signals are not

directly comparable in amplitude, and their sampling rates are different, but they show qualitatively comparable ground vibrations due to digging pulses that rise above ambient background noise.

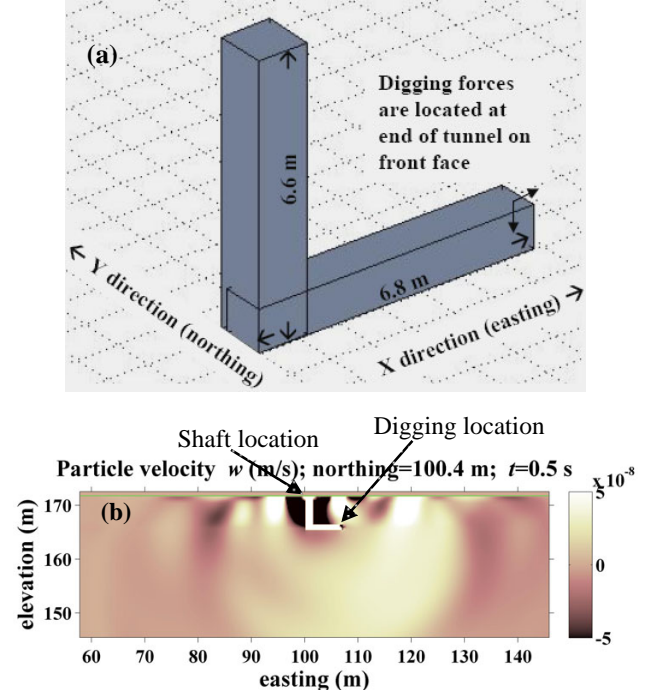


Fig. 1. Flat-terrain tunnel model. (a) Isometric view of tunnel (6.8-m-long with  $1 \times 1$ -m cross section) and vertical shaft (6.6-m-deep with  $1.2 \times 1.2$ -m cross section). (b) Zoomed view snapshot of vertical particle velocity, on cross-section through tunnel, caused by seismic waves from digging pulse. The topographic surface is at elevation = 171.75 m. The color bar is the particle-velocity scale. It has a  $\pm 5 \times 10^{-8}$  m/s range.

Of interest in real-world situations is the ability to discern digging signatures not only in an ambient noise environment, but also in the presence of specific noise sources. We illustrate the ability to simulate such situations in Fig. 3, which shows spectral content of the Fig.-2 digging pulses when ground vibrations are dominated by a nearby harmonic source.

#### 3.2. Propagation from tunnel-digging pulses in urban terrain

The second model is a synthesized urban-terrain model, which is described fully in Ketcham et al. (2005). This model has two central blocks separated by a boulevard with a median and sidewalks. Each central block has four five-story buildings with parking lots in between. Roads and sidewalks surround the central blocks. All buildings have basements. To this model we have added an air-filled unlined tunnel to represent a clandestine tunnel under construction. The tunnel nearly connects two buildings.

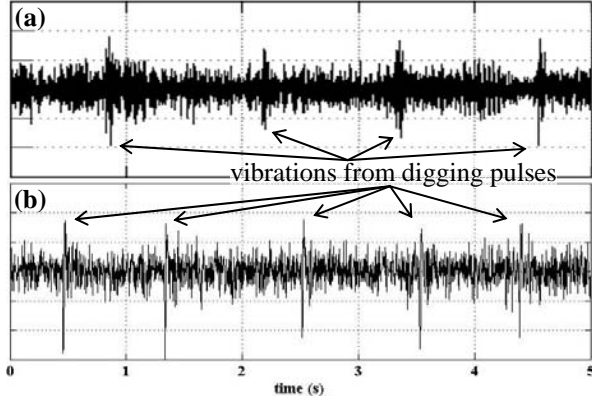


Fig. 2. Comparison of measured and simulated surface ground vibration from hand digging on clay section of tunnel face with  $\sim 1$ -Hz repetitive pulses: (a) experimental and (b) synthetic signals of vertical particle velocity within noise background.

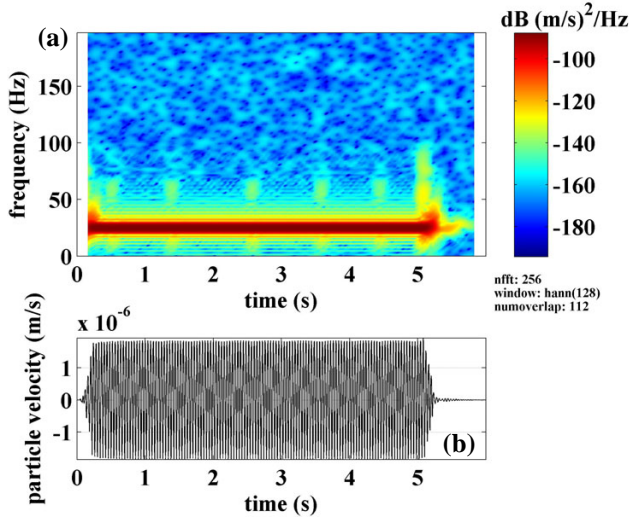


Fig. 3. Vertical ground vibrations from simulated digging pulses in the presence of larger vibrations from 25-Hz generator-induced noise, also from simulation. (a) Spectrogram and (b) signal of the vibrations on surface 35 m south of the digging location. (The 25-Hz source was 20 m east of the digging location). The pulses are faint in the spectrogram, but evident. In the time domain signal they are not apparent.

A vertical shaft from the basement of one building connects to the horizontal tunnel, which is 9 m deep and has a  $2 \times 2$ -m cross section. Figs. 4a and 4b illustrate the urban model and soil layers, and Fig. 4c illustrates the tunnel from a viewpoint below the ground. The soil layers have increasing stiffness with depth, and approximate subsurface layering and material properties at a location within Yuma Proving Ground. We designed the force vectors and time series to approximate seismic excitation caused by digging on the working face with an air hammer, and designed the model grid and source filters to provide accurate wave propagation up to 48 Hz.

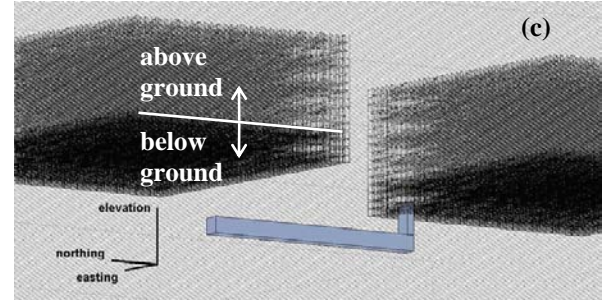
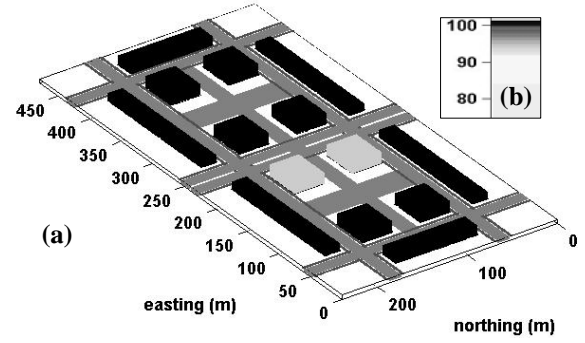


Fig. 4. Urban-terrain tunnel model. (a) View from above, (b) illustration of subsurface-soil layering, and (c) view of tunnel between two buildings, from below the surface. The two buildings with gray (rather than black) highlighting in (a) are those shown in (c).

The excitation history was a 5-s triangular pulse-train with 0.06-s pulses repeating at a mean frequency of 33.3 Hz. Three orthogonal force vectors at the end of the tunnel, with equal magnitude in the positive easting, northing, and elevation directions, combined to produce the resultant forces. Randomness in the application time and the force-resultant amplitude approximated realistic variations of air-hammer operation. The excitations generated surface waves in the ground with predominant wavelengths slightly longer than 10 m. Fig. 5a illustrates the vertical particle velocity wave field over the ground surface. This snapshot shows the complex interaction of the surface waves with the basements of the buildings, and interactions with the pavement structures as well. In the soil just beneath the basements of the buildings, the longer wavelengths within the deeper stiffer soil are evident.

Figs. 5b and 5c plot the response to the excitation at  $\sim 20$  m southwest from the source's lateral position. Fig. 5c shows the time series of vertical particle velocity at this location, while Fig. 5b is a spectrogram that illustrates the evolving frequency-domain power of the signal. The time series reflects the randomness given to the excitation signal, while the high-amplitude line at  $\sim 33$  Hz in the spectrogram shows that the surface waves at the signal location arrive at the mean frequency, and thus with signature characteristics, of the source.



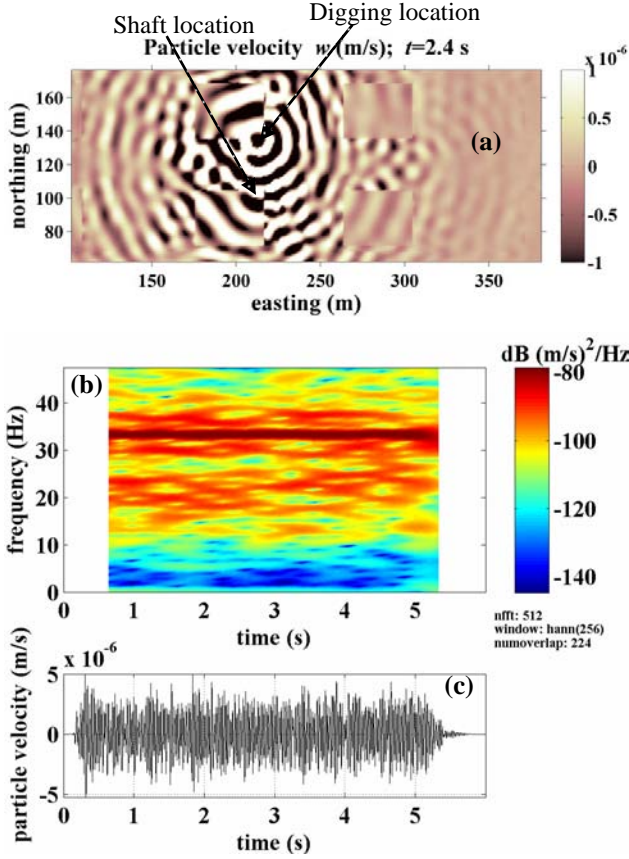


Fig. 5. (a) Zoomed view snapshot of vertical particle velocity, on surface and at base of building foundations, from air-hammer digging pulses. The particle-velocity scale has a  $\pm 1 \times 10^{-6}$  m/s amplitude. Wave amplitudes saturate this scale near the source but reveal the propagation pattern over the domain. (b) Spectrogram and (c) signal of vertical particle velocity at (easting, northing)=(197, 120) m.

### 3.3. Propagation from underground-facility machine vibrations in mountainous terrain

The third model is a synthesized mountainous setting that includes an underground facility adjacent to a campus of buildings that could be apartment buildings, industrial buildings, stores, etc. Like the buildings in the previous model, the foundations of these buildings have sufficient depth (up to 4 m) to affect surface wave propagation. Fig. 6a illustrates the model surface and the locations of the buildings.

The geology of the model (Ketcham et al., 2004) has the surface topography of a mountain gap. Its subsurface consists of a soil basin at lower elevations and bedrock beneath a thin-but-variable-depth soil layer elsewhere. The soil in the basin extends irregularly to a depth as much as 25 m. Softer than the bedrock, the soil produces a large contrast in amplitude and wavelength.

Fig. 6b is a close-up view of the campus and the underground facility. The underground facility is east of

the campus beneath an outcrop of bedrock. It comprises a central multi-story structure and a long tunnel with portals emerging at the ground surface. The facility has walls and floors with material properties similar to concrete and interior spaces with air properties. The east-west tunnel is  $4.5 \times 6 \times 300$  m in dimension at a 600-m elevation. The central facility is  $40 \times 40$  m in plan. It has three floors, each with 4.5-m ceilings. The lowest floor is at elevation 595 m. Within this floor we introduced a time-varying vertical force to approximate the excitation of a harmonically vibrating machine on a slab.

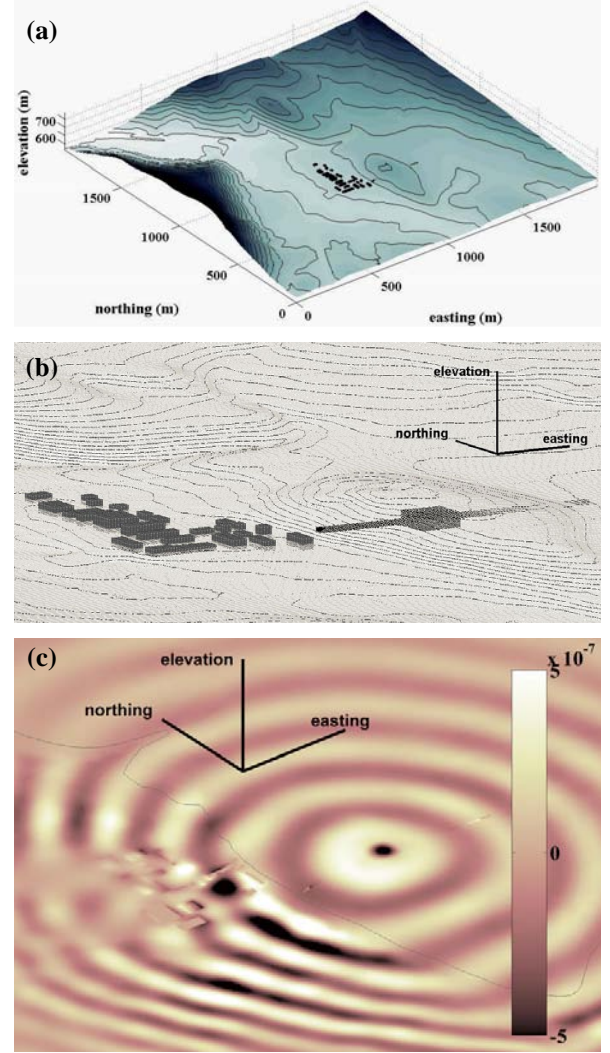


Fig. 6. Mountainous-terrain underground-facility model. (a) View of topographic surface with building locations, (b) close-up view of buildings and adjacent underground facility beneath outcrop, and (c) zoomed view snapshot of vertical particle velocity (m/s) on surface from machine-induced harmonics. The limits of the particle-velocity scale are  $\pm 5 \times 10^{-7}$  m/s.

We discretized the model to analyze surface wave propagation for sources having frequency content less than 25 Hz. Accordingly, we created the source with

superimposed 7.5- and 15-Hz forces. These forces resulted in a harmonic vertical excitation of  $\pm 15$  kN at a depth 26 m below the topographic surface.

Fig. 6c illustrates surface waves spreading from the source over the topography. The predominant features of the snapshot are the bull's eye pattern of propagation, the shortening of the wavelengths in the soil basin (to the left of the underground facility), and the turbulence-inducing effect that the building basements have on the passing waves.

### 3.4. Spatial processing of relative energy and normalized cross correlation

We are currently researching the post-processing of simulated wave-field signals to calculate spatial measures of relative energy and normalized cross correlation. Our objective is to map these measures to view regions of relatively high and low signal amplitude and similarity, and to examine the effect of complex propagation environments on optimal sensor placement for detection, signature, and array-processing analyses. Here we present calculations of these measures from responses of the mountainous- and urban-terrain models to broadband-pulse excitations. We derive frequency-response functions for the surface nodes, and characterize the viscoelastic systems excited previously by air-hammer-digging and machine-induced-harmonic forces, respectively. In effect, we perform a trial of the spatial measures as decision-support tools for sensor placement

Figs. 7a and 8a illustrate a measure of normalized or relative energy over the surfaces of the mountainous- and urban-terrain models. The measure is derived from the frequency response function between the broadband input signal and the output signal at each node location on the model surface, which we designate  $H(x, y, f)$ , where  $x$ ,  $y$  and  $f$  are discrete values of easting and northing coordinates and frequency, respectively. Our signal processing code calculates the frequency response function as the ratio of the Fourier transforms of the output signals to the Fourier transform of the excitation signal.

Using  $H(x, y, f)$ , which also equals the discrete Fourier transform of the system's impulse response function, the processing code calculates the average energy spectral density of the impulse response over frequency bands of interest. For example, the calculation in Fig. 7a is for the frequency band [13.5, 15.7] Hz, which spans the highest-frequency harmonic of the machine-vibration excitation in the mountainous-terrain model. The code calculates in-band energy, average in-band energy, and finally the relative energy, which we describe here in successive steps. The in-band energy is:

$$G(x, y, \hat{f}) = H^*(x, y, \hat{f})H(x, y, \hat{f}) \quad (1)$$

where  $\hat{f} \equiv [f_a, f_b]$  designates the discrete frequencies from  $f_a$  to  $f_b$  and  $*$  denotes the complex conjugate. The average in-band energy is:

$$\bar{G}_{\hat{f}}(x, y) = \frac{1}{f_b - f_a} \sum_{f=f_a}^{f_b} [G(x, y, \hat{f})\Delta f] \quad (2)$$

where  $\Delta f$  is the discrete-frequency difference. The relative energy, designated  $\tilde{G}_{\hat{f}}(x, y)$ , is:

$$\tilde{G}_{\hat{f}}(x, y) = \frac{\bar{G}_{\hat{f}}(x, y)}{\text{median}[\bar{G}_{\hat{f}}(x, y)]_{r_a}^{r_b}} \quad (3)$$

where the median calculation of the denominator includes all  $x$ ,  $y$  positions whose distance from the source epicenter are within the annular radii  $r_a$  and  $r_b$ ; and the  $x$ ,  $y$  position of the numerator solution point is within this annulus. For Figs. 7a and 8a we chose  $\Delta r$  of the radii to be less than two grid-node spacings. As Eq. 3 indicates, to calculate relative energy, the code divides the average in-band energy at each  $x, y$  point by the median of all like values within a narrow annulus from the source epicenter. The annulus includes the point  $x, y$ , and so the effect is that distance from the source is removed as a variable.

Calculating  $10 \times \log(\tilde{G}_{\hat{f}}(x, y))$  allows for plotting on a decibel scale, with  $\pm 10$  dB spanning an order of magnitude. Using a green-yellow-red color bar on the decibel scale produces a spatial plot where, at equal distance from the source, green locations have the highest energy in the frequency band, i.e., the highest amplitude, and red locations have the lowest.

Figs. 7b and 8b illustrate a measure of the normalized cross correlation of signals separated by a given distance, respectively, for the mountainous- and urban-terrain models. To derive the normalized cross correlation for each node point, the processing code first locates  $n$  pairs of signals from opposite points around a circle that is centered at the node point. The  $2n$  total signal locations are equally spaced and thus separated by  $\pi/n$ . This circle has diameter  $d$ . The processing provides a spatial measure of similarity for signals separated by less than the distance  $d$ .

Using band-limited signals within  $\hat{f} \equiv [f_a, f_b]$ , we designate the cross and auto correlation time series by  $R_{kl\hat{f}}(x, y, t)$ ,  $R_{kk\hat{f}}(x, y, t)$ , and  $R_{ll\hat{f}}(x, y, t)$ , where  $x$  and  $y$  define the center of the circle and  $k$  and  $l$  designate the two points of a signal pair. The processing code calculates the maximum of the cross correlation for each signal pair and divides this by the product of the auto-correlation maxima, which occur at  $t = 0$ . The average of these  $n$  calculations is the normalized cross correlation  $\tilde{R}_{\hat{f}}(x, y)$ , i.e.,



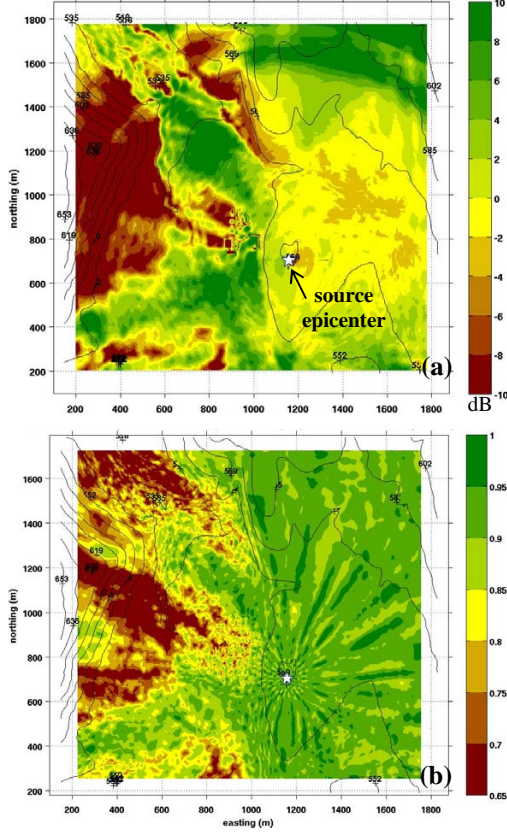


Fig. 7. Images of (a) relative energy (dB) and (b) normalized cross correlation for the mountainous-terrain underground-facility model. The calculations are for the frequency band [13.5, 15.7] Hz. The cross correlation calculations, at each plotted location, used four signal pairs with a spatial separation of 120 m.

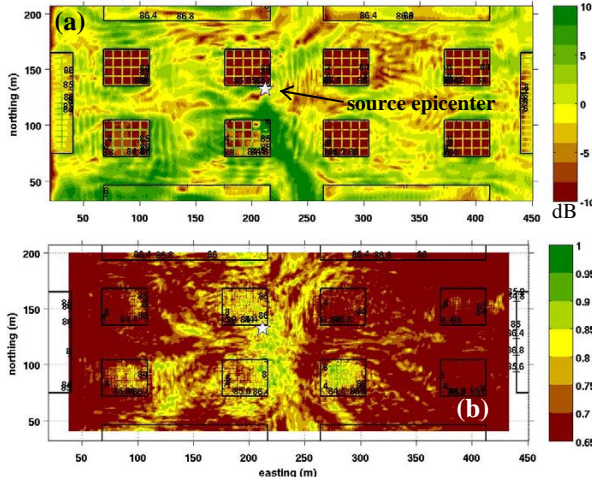


Fig. 8. Images of (a) relative energy (dB) and (b) normalized cross correlation for the urban-terrain tunnel model. The calculations are for [29.8, 37.3] Hz. The correlation calculations used four signal pairs at 13.2 m separation.

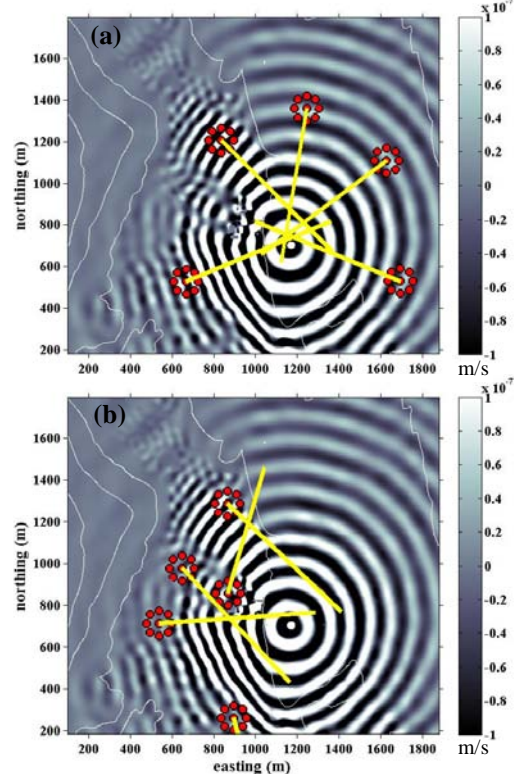


Fig. 9. Array configuration and locations (red circles), and beam directions (yellow lines) formed by beam-forming algorithm, for array placements in areas of (a) high and (b) low relative energy and normalized cross correlation, plotted on a snapshot of vertical particle velocity from the mountainous-terrain underground-facility model. The limits of the particle-velocity scales are  $\pm 1 \times 10^{-7}$  m/s.

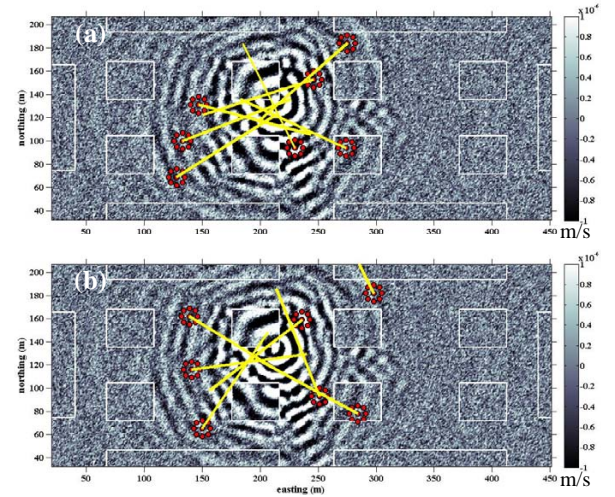


Fig. 10. Arrays (red circles) and beam directions (yellow lines) for arrays in areas of (a) high and (b) low relative energy and normalized cross correlation, plotted on a snapshot of vertical particle velocity with noise from the urban-terrain tunnel model. The limits of the particle-velocity scales are  $\pm 1 \times 10^{-6}$  m/s.

$$\tilde{R}_{\hat{f}}(x, y) = \frac{1}{n} \sum_{k=1}^n \left( \frac{\max[R_{kl\hat{f}}(x, y, t)]}{\sqrt{R_{kk\hat{f}}(x, y, 0)R_{ll\hat{f}}(x, y, 0)}} \right) \quad (4)$$

where the points  $k$  and  $l = k + n$  are sequential counterclockwise points on the circle each subtending arc-length  $\pi$ . The values of  $\tilde{R}_{\hat{f}}$  can fall between 0 and 1.

We note a related use of normalized cross correlation in (Mykkeltveit et al., 1983), in which cross-correlation data were applied to estimate optimal array configurations.

While Eq. 4 indicates time-domain functions, our calculations of  $\tilde{R}_{\hat{f}}$  are in the frequency domain (Bendat and Piersol, 1986), beginning with  $H(x, y, f)$  extracted from  $\hat{f} \equiv [f_a, f_b]$ . The processing calculates cross and auto spectra of the band-limited impulse response at the signal locations, and inverts to the time domain to arrive at the needed correlations.

We plot the result using a green-yellow-red color-bar scale between 0.65 and 1, selecting a cutoff below 0.7 to indicate signal dissimilarity that adversely affects array processing. Green locations have the highest normalized cross correlation for the given signal separation and frequency band, and red locations have the lowest. Note that processing with a limited number of signal pairs at each  $x, y$  point introduces bias errors in the plotted images, especially close to the epicenter. Fig. 7b shows this bias to have an effect on normalized-cross-correlation values calculated with four signal pairs, producing a radial pattern centered above the source location. Flat-layered models show this effect to be slight, reducing some values where  $\tilde{R}_{\hat{f}} = 1$  to approximately 0.95.

Examining the plots of these measures in Figs. 7 and 8, we can look for regions with both relatively high amplitude and normalized cross correlation within the frequency band to support sensor locations for array processing. For example, in Fig. 7a, the effect of the building foundations on the amplitude of waves propagating from the underground facility is evident in the red-colored region to the north and west of the building campus, which is in the otherwise high-amplitude setting of the soil basin. Similarly, this area is a region of low normalized cross correlation, as indicated by Fig. 7b. Thus both the relative energy and normalized-cross-correlation measures are quantitative indications of the negative impact of the building foundations on seismic sensing in this region.

Relative energy for the urban tunnel model reveals the effect of its buildings on propagation from the tunnel. The calculations spanned the frequency band  $\hat{f} \equiv [29.8, 37.3]$  Hz, which encompassed the air-hammer pulse frequency of the model. Fig. 8a shows the capacity of building foundations to obstruct and direct energy in this band, which is evident in red- and green-colored regions, respectively. Fig. 8b shows the severe impact that

urbanization, and also the complexities of propagation along the tunnel, can have on the normalized-cross-correlation values. The values are low over most of the model surface, with the highest values close to the tunnel.

For Figs. 7b and 8b, we prepared the normalized-cross-correlation maps using spatial separations of 120 and 13.2 m, respectively. We chose these separations to be slightly greater than the wavelengths of the dominant waves in the previous analyses of machine vibrations and tunnel digging for two reasons: (1) our intended application of the maps was to quantify optimal array positions for frequency-wavenumber (f-k) beam-forming analyses; and (2) the array diameter for beam-forming applications should be at least the length of the longest waves of interest (e.g., Rost and Thomas, 2002). Using Figs. 7 and 8 we formed networks of beam-forming arrays by placing the arrays in “good” areas, i.e., areas with relatively high amplitude  $\tilde{G}_{\hat{f}}$  and normalized cross

correlation  $\tilde{R}_{\hat{f}}$ . These locations are shown in Figs. 9a and 10a. We also placed arrays in “bad” areas with relatively low amplitude and normalized cross correlation. Figs. 9b and 10b plot these arrays. As illustrated, all arrays comprised eight locations on the circles (with either 120- or 13.2- m diameter) plus the center point.

In addition to the array locations, Figs. 9 and 10 plot the resulting beams at snapshots in time superimposed on respective images of the wave field from the mountainous-terrain underground-facility model and the urban-terrain tunnel model. We processed these beams using a maximum-slowness f-k algorithm (Hart and Young, 2004). The Fig.-9a arrays, which are from locations with high relative energy and normalized cross correlation in the mountainous-terrain underground-facility model, show beams from each array reliably pointing in the direction of the local wave arrivals. The beams also point toward the source epicenter, but with bias errors that derive from geology-induced wave refractions. Without correcting for these refractions (Moran et al., 2001), source-location estimates will reflect these errors. Depending on the accuracy requirement, a source-location estimate from the Fig.-9a beams may or may not be satisfactory. We applied a median-line-crossing algorithm to these and other beams calculated in a sliding window analysis, which estimated the source location to within 53-m accuracy, or 9 percent relative error when normalizing by mean distance between the source and the arrays. In contrast, the relative error using the Fig.-9b beams was greater than 75 percent.

In our research, we plan to use  $\tilde{G}_{\hat{f}}$  and  $\tilde{R}_{\hat{f}}$  with measurements and estimates of noise power to examine the effects of complex geology, urban features, and noise on sensor placement and performance as source and noise levels vary in time. As a precursor to this work, we superimposed ambient noise onto the signals used for the beam-forming analyses illustrated in Figs. 10a and 10b.



The signals are from the simulation of air-hammer digging in the urban-terrain tunnel model. The figures show beams from arrays placed in “good” and “bad” sensing locations, respectively. The wave field is depicted with superimposed random ambient noise. The median-line-crossing algorithm, using beams from the Fig.-10a arrays, estimated the source location to within 5.8 m accuracy (8 percent relative error), compared to 9.3 m (13 percent relative error) as the best estimate using the Fig.-10b “bad”-location arrays. While this contrast in accuracy is not as striking as the previous example, both examples show that network source-location performance improves by locating sensors where both amplitude and signal-similarity measures are relatively high.

## CONCLUSIONS

Results from seismic simulations of wave propagation from dynamic activity in tunnels, which we have simulated in open, urban, and mountainous terrain, reveal the pulsating nature of seismic waves as they emanate from digging pulses and harmonic vibrations. We find that time-domain characteristics of our simulated open-terrain signals compare well with field signals. In mountainous and urban settings, results show the effect of geology and urban infrastructure on propagation from digging-pulse and machine-foundation sources in tunnels and underground facilities. Our spatial post-processing of relative energy and signal cross correlation from models in mountainous and urban environments provides maps of optimal sensor performance in these model domains. Application of these maps is shown to improve the accuracy of source location by beam forming. We conclude that the HPC seismic simulation method produces realistic wave-field data, at scales of interest for DoD applications, for virtual trials of sensing algorithms and development of sensor-array decision-support tools.

## ACKNOWLEDGEMENTS

Funding support is from DoD High Performance Computing Modernization Program (HPCMP) Software Applications Institute I-01: Institute for Maneuverability and Terrain Physics Simulation; USAERDC Program URBAN; USA Rapid Equipping Force; and Quantum Technology Services, Inc., via Cooperative Research and Development Agreement “FDTD Modeling for QTSI Seismic Network Development.” Computational support is from HPCMP Project ERDCH11304ERD.

## REFERENCES

Bendat, J.S. and Piersol, A.G., *Random Data, Analysis and Measurement Procedures*, 2nd ed., John Wiley, New York, 1986.

- Cerjan, C., Kosloff, R., and Reshef, M., A Nonreflecting Boundary Condition for Discrete Acoustic-Wave and Elastic-Wave Equations, *Geophys.*, SEG, Vol. 50, 1985, pp. 705-708.
- Defense Advanced Research Project Agency (DARPA), Passive, Acoustic, Seismic and Electromagnetic Monitoring (PASEM), Special Projects Office Website, Accessed June, 2006, <http://www.darpa.mil/spo/programs/pasem.htm>.
- Fainaru, S. and Shadid, A., In Iraq Jail, Resistance Goes Underground, *Washington Post*, August 24, 2005, pp. A01.
- Hart, D. and Young, C., *MatSeis User's Manual*, Ver. 1.9, Sandia National Laboratories, Albuquerque, 2004.
- Ketcham, S.A., Moran, M.L., and Lacombe, J., Seismic Waves from Light Trucks Moving Over Terrain, Proc. 2004 Users Group Conference, DoD High Performance Computing Modernization Program, IEEE Computer Society, pp. 65-70.
- Ketcham, S.A., Lacombe, J., Anderson, T.S., and Moran, M.L., Seismic Propagation from Humans in Open and Urban Terrain, Proc. 2005 Users Group Conference, DoD High Performance Computing Modernization Program, IEEE Computer Society, 2005, pp. 270-277.
- McKenna, J.R., Assessment of Seismic-Acoustic Techniques for Tunnel Detection, ERDC Technical Report, in review, 76 pp., 2006.
- McKenna J.R. and McKenna, M.H., Effects of Local Meteorological Variability on Surface and Subsurface Seismic-Acoustic Signals, in review, *Geophysical Research Letters*, 2006.
- Moran, M.L., Greenfield, R.J., and Ketcham, S., Geologic Adaptation for Seismic Network Tracking, Proc. 2001 MSS Battlefield Acoustic and Seismic Sensing, Magnetic and Electric Field Sensors, paper G05, Conference CDROM, vol. II, 2002.
- Mykkeltveit, S., Åstebøl, K., Doornbos, D.J., and Husebye, E.S., Seismic Array Configuration Optimization, *Bull. Seis. Soc. Am.*, SSA, Vol. 73, 1983, pp. 173-186.
- Rost, S. and Thomas, C., Array Seismology: Methods and Applications, *Rev. Geophysics.*, AGU, Vol. 40, 2002, pp. 2-1-2-27.
- Rowe, R.J., Statement of Major General Richard J. Rowe, Jr., USA, Director of Operations [J-3, United States Northern Command], Before the House Armed Services Committee, on Use of the National Guard to Support Border Security, US House of Representatives Website, Accessed June, 2006, <http://www.house.gov/hasc/schedules/5-24-06RoweTestimony.pdf>.
- Sabatier, J.M. and Muir, T.G., Workshop on Real-Time Detection of Clandestine Shallow Tunnels, National Center for Physical Acoustics, Univ. of Mississippi, NCPA Report HB0306-01, US Army Research Office, Grant No. W911NF-06-1-0001, April, 2006.